

CHAPTER 5
ELECTRO-OPTIC PROPERTIES OF
BULK AND NANOSTRUCTURED
ALUMINIUM Pnictides

5.1 Introduction

The semiconductors acquire the paramount position in the present cutting-edge technologies due to their versatile nature and promising properties.¹⁻⁴ Apart from carbon-based materials, the III-V compounds share the top position in the nanoelectronics and nanodevice industry.^{5,6} The journey started with gallium and indium-based arsenide materials, and following the ladder, the invention of blue light emitting diode (LED) via incorporation of lighter group V compounds in conventional III-V materials became the ground breaking contribution to the device industry.⁷ However, the nanowire (NW) configurations of these semiconductors were not studied, until the successful nucleation of GaAs and InAs nanowhiskers below 100 nm was made possible by a research group at Hitachi Central Research Lab.⁸ This led to the first successful demonstration of the functional LEDs made of GaAs NWs, that with the realization of the formation of heterostructure.⁹ As far as aluminium is concerned, the Al-V materials have been explored under various geometric aspects, for their fundamental and applicative properties,¹⁰⁻¹⁶ yet a systematic investigation on the aluminium phosphide (AlP) and aluminium arsenide (AlAs) ranging from their bulk crystal phases to the two-dimensional confined configuration (nanowire) to the complex nanostructured geometry was missing. However, the AlP and AlAs compounds have been significantly studied under alloyed/heterostructured configuration for various device applications.^{14,17-20} Unlike other elements from boron group, the aluminium being the third most abundant element in earth's crust draws significant attention due to its advantages like low cost, light weight, high corrosion resistance, flexibility and non-toxic nature. These numerous advantages of aluminium

and its benchmarking properties when combined with group V elements makes it necessary to study these materials in depth. It is evident from the reports that the III-V materials prefer cubic zincblende (ZB) phase under bulk and hexagonal Wurtzite (WZ) phase under confined conditions,²¹⁻²³ the fundamental studies^{13,24,25} reporting the ground state properties of these compounds under WZ phase provided fruitful insight to the dramatic differences in the phase dependent properties. Under ambient conditions, except AlN, remaining all Al-V compounds possess cubic ZB phase and an electronic band gap lying within optical spectral range.²⁶ Versatile nature with diverse applications, and the necessity to understand the energetics of the AlX (X=P/As) compounds under different configurations worked as a fuel for the present study. We have explored AlP and AlAs compounds under two bulk polytypic phases; (i) cubic zincblende (ZB) and, (ii) hexagonal Wurtzite (WZ). Followed by the investigation of electronic, optical and vibrational properties of these materials under bulk configuration, the two-dimensional quantum confinement is applied on these materials to construct one-dimensional (1D) nanowires (NWs), and the electro-optic properties under the confined condition are investigated. At the end, the two NWs were utilized for the construction of the 1D radial and axial heterostructure nanowires (HSNWs), and the same were considered for studying the modulation in the electro-optic transport properties due to the complex structural configuration. The *state-of-art* transport governing factors under bulk and nano regime are very sensitive to the size effects and hence crucial to understand for drawing a crystal-clear pathway connecting the bulk and nano properties.

5.2 Computational Details

The aluminium pnictides AlX (X=P, As) with cubic zincblende (ZB) and hexagonal Wurtzite (WZ) bulk phases and their nanostructured configurations were studied within the *state-of-art* density functional theory (DFT)²⁷ framework. Primary optimization of the bulk unit cells was done utilizing the self-consistent total energy minimization process. The local density approximated pseudopotentials with plane-wave basis sets were incorporated for describing the atomic cores and valence electron configuration.²⁸ The optimized kinetic energy cut-off of 1600 eV and the Monkhorst-Pack scheme²⁹ based k-mesh grids of 16x16x16 and 16x16x10 respectively for ZB and WZ bulk phases were found sufficient to converge the total energy and forces per atom within the threshold magnitudes. The lattice parameters of the systems were optimized upto the third decimal place (see Table 5.1). Following this, the optimized unitcells were considered for investigating the ground state electronic and optical properties. As mentioned earlier, the electronic band structure of the systems are computed within pseudopotential approach, and, utilizing the random phase approximation (RPA),^{30,31} the respective optical transport through the systems was calculated. For the construction of the NWs the optimized crystal structures of bulk AlP and AlAs were repeated so as to form a 6x6 supercell, and NWs with desired diameter were then cut from them in such a way that the growth direction coincides with the 0001 direction. The unsatisfied valency of the surface atoms of the NWs were saturated by passivating the surfaces of the NWs with hydrogen adatoms. The so prepared passivated NWs were then fully relaxed till the convergence conditions were not satisfied. Akin to the bulk phases, the electro-optic transport under NW

configuration was also investigated so as to get insight to modifications subjected to quantum confinement. Followed by this, the last step was to construct heterostructures (HS) from these NWs and to unravel their electro-optic properties. HSNWs with radial and axial configurations were studied so as to draw a clear picture of geometry dependence modulations in the electro-optic transport properties of AlX compounds. The kinetic energy cut-off and k-mesh grids under NW and HSNW configurations were kept at 1630 eV and 1x1x8 respectively for obtaining ground state electronic wave-function, and, for calculating optical properties much denser k-mesh grids were set. Prior to computation of the ground state properties of the systems, the stability of the systems was confirmed by means of computing cohesive energy.

$$E_{Coh}^{BULK} = \left(\frac{(n_{Al}\mu_{Al} + n_{P/As}\mu_{P/As}) - (E_{Total}^{Unit})}{N} \right) \quad (5.1)$$

$$E_{Coh}^{NW} = \left(\frac{(n_{Al}\mu_{Al} + n_{P/As}\mu_{P/As} + n_H\mu_H) - (E_{Total}^{NW})}{N} \right) \quad (5.2)$$

$$E_{Coh}^{HSNW} = \left(\frac{(n_{Ga}\mu_{Ga} + n_{Sb}\mu_{Sb} + n_X\mu_X + n_H\mu_H) - (E_{Total}^{HSNW})}{N} \right) \quad (5.3)$$

The equations (1), (2) and (3) are used for calculating the cohesive energy of the bulk, NW and HSNW configurations respectively. The terms n and μ represent the number and chemical potential of the respective element, with total number of atoms of including all atomic species is represented by N . E_{Total}^{Unit} , E_{Total}^{NW} and E_{Total}^{HSNW} are the corresponding total-energy of the systems under bulk, NW and HSNW configurations. It is to be noted that the equations above do not account for contributions from the vibrational energy of the system.

5.3 Results and Discussion

5.3.1 From bulk to Nanowire

5.3.1.1 Structural Properties

The structural properties of the AlX compounds computed under DFT based self-consistent total energy minimization approach are presented in Table 5.1, and respective structural analogues of the compounds are presented in Figures 5.1 and 5.2. As expected, the computed lattice parameters of the compounds show increase with increase in anion mass subjected to the modification in the atomic radii. It is noteworthy, that the computed parameters are in good agreement with the reported experimental and theoretical data.³² In case of WZ compounds, we could not compare the results as these compounds under bulk condition prefer ZB phase.

Table 5.1. Computed structural and electronic parameters of AlX (X=P, As) in bulk, nanowire (NW) and radial (R) and axial (A) heterostructure nanowire (HSNW) configurations.

System	Phase	Lattice Parameter (Å)	Cohesive Energy (eV)	Valence band maxima (eV)	Conduction band minima (eV)	Electronic bandgap E_g (eV)	Nature
AlP Bulk	ZB	5.402	5.534	5.102	6.498	1.395	I
	WZ	6.264	5.531	5.213	6.993	1.780	I
AlAs Bulk	ZB	5.606	5.071	4.864	6.215	1.350	I
	WZ	6.502	5.066	4.971	6.647	1.675	I
AlP NW	WZ	6.138	4.808	-3.466	-0.716	2.749	D
AlAs NW		6.508	4.491	-3.296	-0.682	2.614	I
AlP/AlAs (R)	WZ	6.270	4.568	-3.248	-0.649	2.598	I
AlAs/AlP (R)		6.297	4.734	-3.373	-0.660	2.713	D
AlP/AlAs (A)		12.515	4.652	-3.345	-0.606	2.739	D

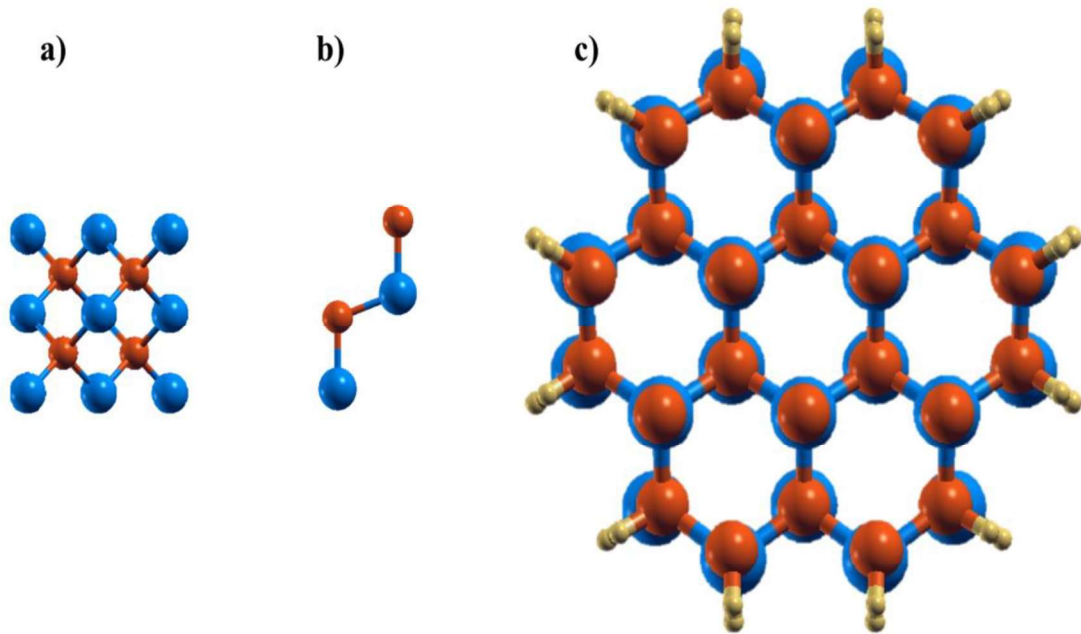


Figure 5.1. Optimized crystal structures of aluminium phosphide (AlP) in bulk (a) cubic zincblende (ZB) and (b) hexagonal Wurtzite (WZ), and (c) nanowire (NW) Phases. The spheres in blue, brown and yellow represent the atoms of aluminium, phosphorous and hydrogen, respectively.

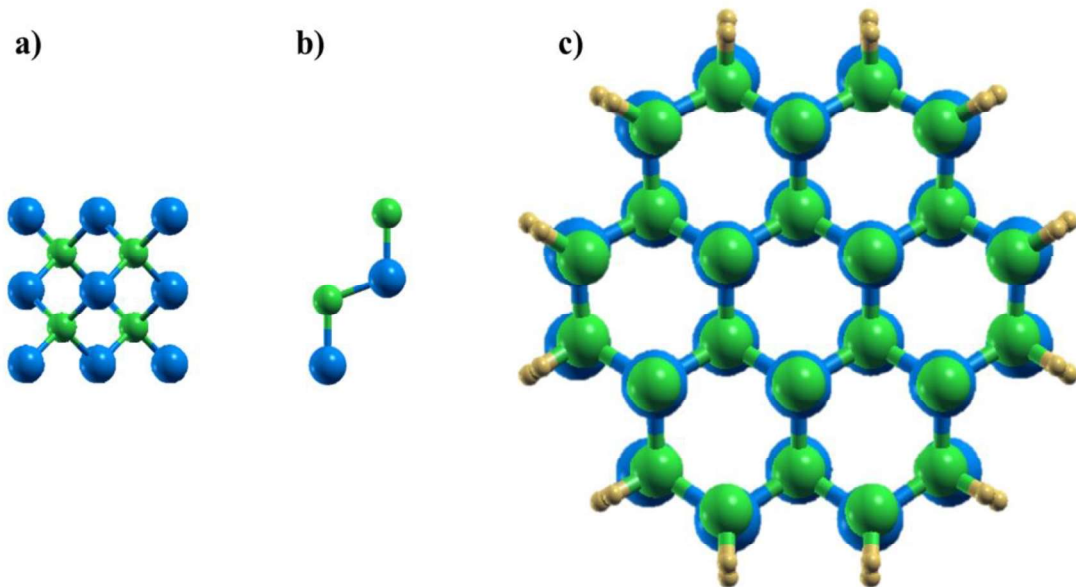


Figure 5.2. Optimized crystal structures of aluminium arsenide (AlAs) in bulk (a) cubic zincblende (ZB) and (b) hexagonal Wurtzite (WZ), and (c) nanowire (NW) Phases. The spheres in blue, green and yellow represent the atoms of aluminium, arsenic and hydrogen, respectively.

As mentioned earlier, the energetic stability of the systems is assessed by calculating the energy of cohesion using equations (5.1), (5.2) and (5.3) for different conditions. Comparing the bulk polytypic phases, we can see that the difference in energy of cohesion due to polytypic phases is negligible; however, positive magnitudes of energy are sufficient to prove the strong covalent nature between the crystal atoms that also make the system energetically stable. Moving towards the NW configuration, we can observe that the NWs are also energetically stable with positive yet slightly lower magnitude of energy of cohesion than the bulk counterparts.

5.3.1.2 Electronic Properties

Moving towards the electronic properties the electronic band structure of the AIP and AIAs under bulk and NW configurations are presented in Figs. 5.3 and 5.4. It is observed that both compounds under two polytypic phases possess indirect nature with a bandgap lying within the range 1.3-1.6 eV. In contrast to this, the NW configurations of both compounds possess slightly large bandgap magnitude of 2.74 and 2.61 eV for AIP and AIAs NW, respectively. As expected, the gap magnitude for AIAs NW is quite lower than the AIP NW due to the inverse correlation between the lattice parameter and the electronic bandgap which is intact in case of bulk counterparts (see Table 5.1). Apart from the gap magnitude, it is important to observe that the effect of quantum confinement does not alter the nature of the bandgap in case of AIP; however, in case of AIAs, the electronic dispersion transits from indirect to direct on imposing two-dimensional quantum confinement (see Fig. 5.4). For optoelectronic and photovoltaic devices, it is of utmost importance that the electronic and optical bandgaps are alike, i.e. a direct bandgap, which in case of AIAs NW is

observed. Further insight to optical transport can be achieved by calculating the absorption co-efficient of the systems.

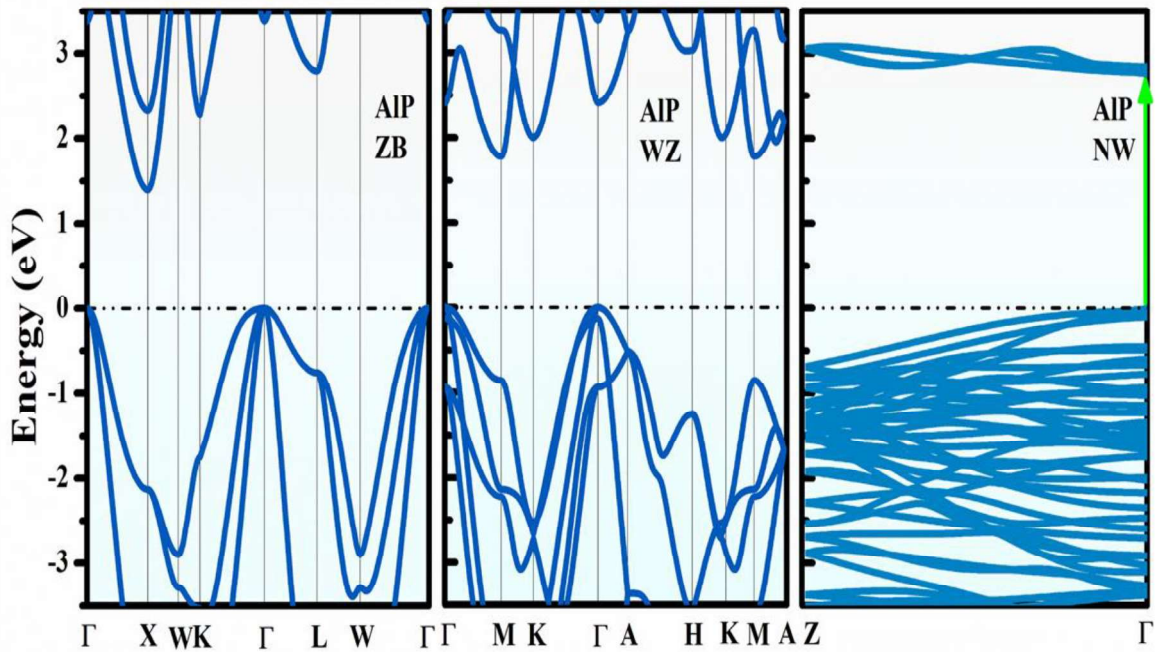


Figure 5.3. Electronic dispersion curve for aluminium phosphide (AlP) in cubic zincblende (ZB), hexagonal Wurtzite (WZ) and nanowire (NW) configurations.

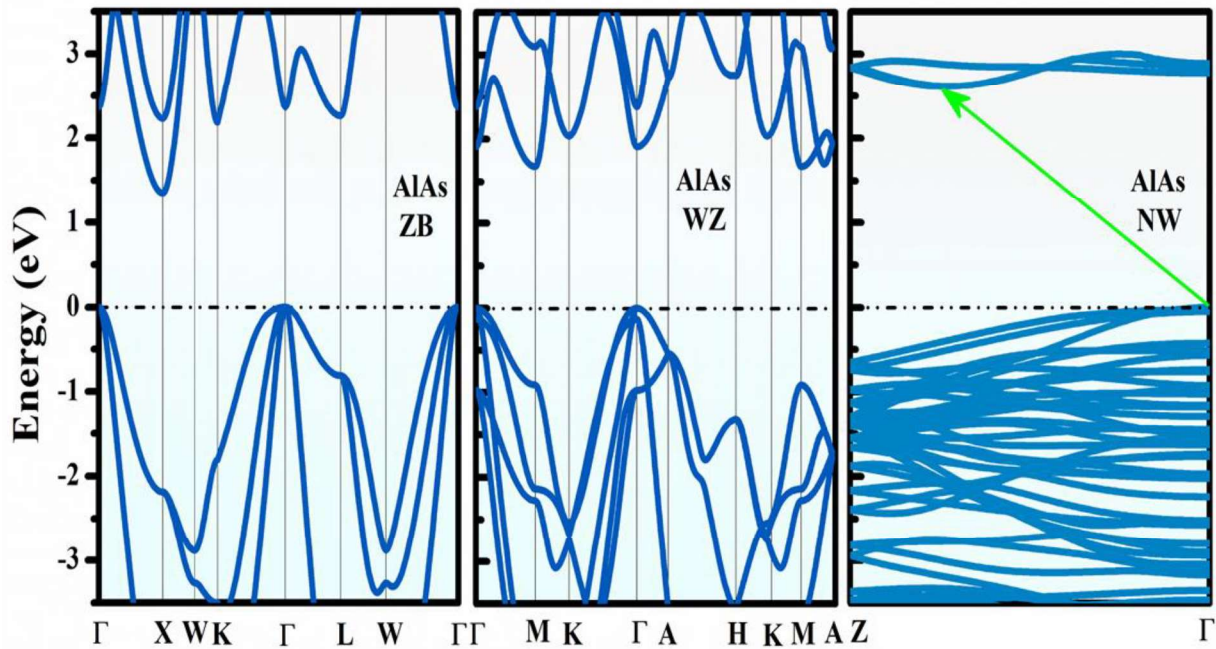


Figure 5.4. Electronic dispersion curve for aluminium arsenide (AlAs) in cubic zincblende (ZB), hexagonal Wurtzite (WZ) and nanowire (NW) configurations.

5.3.1.3 Dynamical Properties

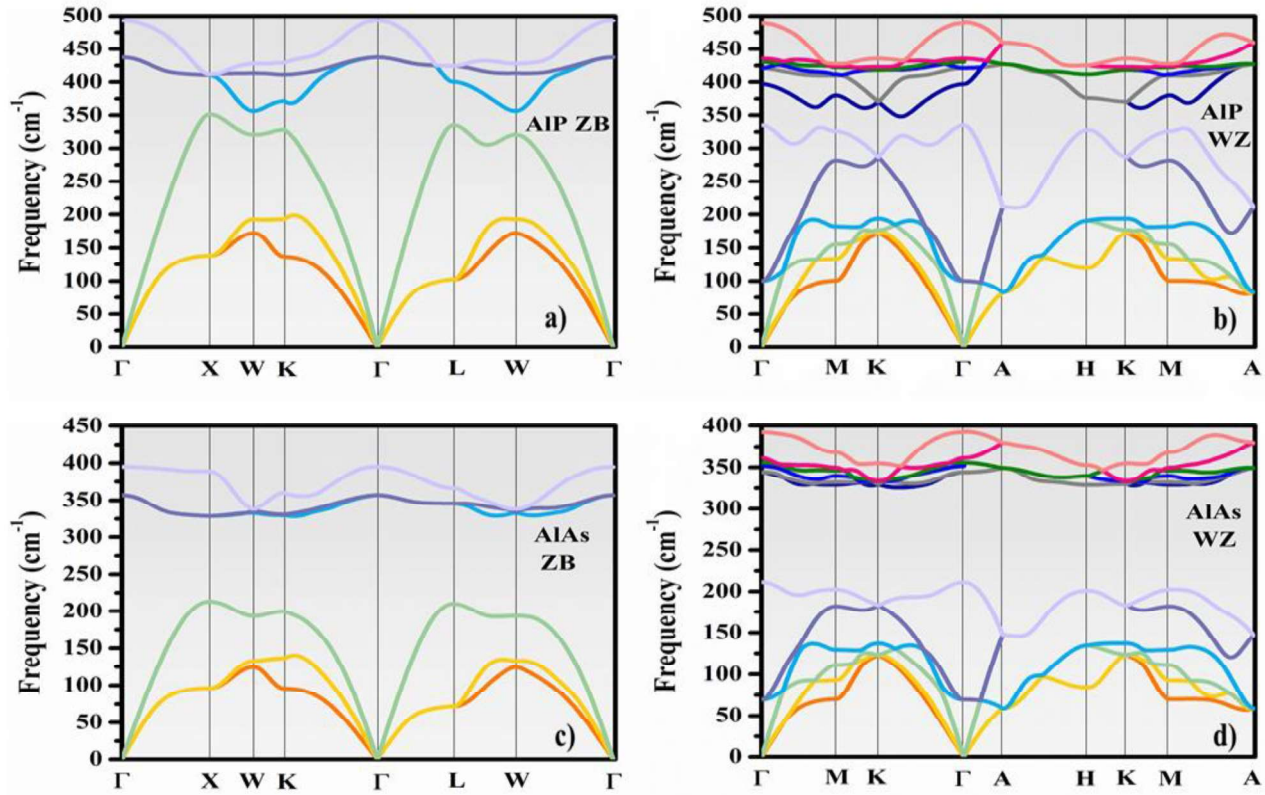


Figure 5.5. Phonon dispersion curve for aluminium phosphide (AIP) and aluminium arsenide (AIAs) in cubic zincblende (ZB) and hexagonal Wurtzite (WZ) phases.

It is expected that the crystal phase which requires minimum energy of formation or high energy of cohesion should remain energetically, dynamically and mechanically stable at ambient conditions. In case of the present compounds AIP and AIAs being from the famous III-V group compounds possess dual polytypic phases; ZB and WZ with cubic and hexagonal symmetries, respectively. We therefore, investigated the dynamical stability of these compounds under polytypic configurations, and as it can be observed from Figure 5.5, both compounds possess stable dynamic configurations. The absence of soft phonon modes or any imaginary components of vibrational frequency in the phonon dispersion curves (PDCs) support this observation. Further, as reports suggest that the WZ phase with hexagonal symmetry under confined

geometry is likely to be much more stable than the ZB phase, we have considered the hexagonal WZ phase only for studying the systems under confined configuration. The dispersive nature and number of phonon branches reveal the role of symmetry and crystal phase in dynamic stability. The longitudinal optic (LO) and transverse optic (TO) phonon modes possess significantly large splitting (see Fig. 5.5) indicating their capability of interacting with high-energy photons. Comparing the acoustic phonon modes of both phases, it is clearly observed from the PDCs that the ZB phase possesses much more pronounced acoustic phonon modes with steep dispersion along the high-symmetry path of the Brillouin zone indicating large group velocity and hence, enhanced thermal conductivity. The WZ compounds on the other hand possess shallow dispersion in case of acoustic phonon modes suggesting much lower thermal conductivity than the ZB counterparts. However small yet unavoidable contribution from the optical phonon modes to the thermal conductivity cannot be neglected, and hence, for qualitatively differentiation full-proof assessment of thermal transport is mandatory. In present case, our motto is to understand the electro-optic profiles of both compounds, therefore we limit the investigation and discussion to electro-optic properties only.

5.3.1.4 Optical Properties

After confirming the dynamical stability of the AlX compounds, we now focus on the optical properties of the compounds under bulk and NW configurations. Figs. 5.6 (a) and (b) present the RPA computed real and imaginary components of complex dielectric function for ZB, WZ and NW configurations. The imaginary part of the complex dielectric function accounts for the absorption capability of the material

which suggests a possibility of optical absorption within the optical range of electromagnetic spectrum for AlX compounds under ZB and WZ phases, while in case of NW configurations, these systems show possibility of absorption within ultraviolet regime (see Figs. 5.6(b) and (d)).

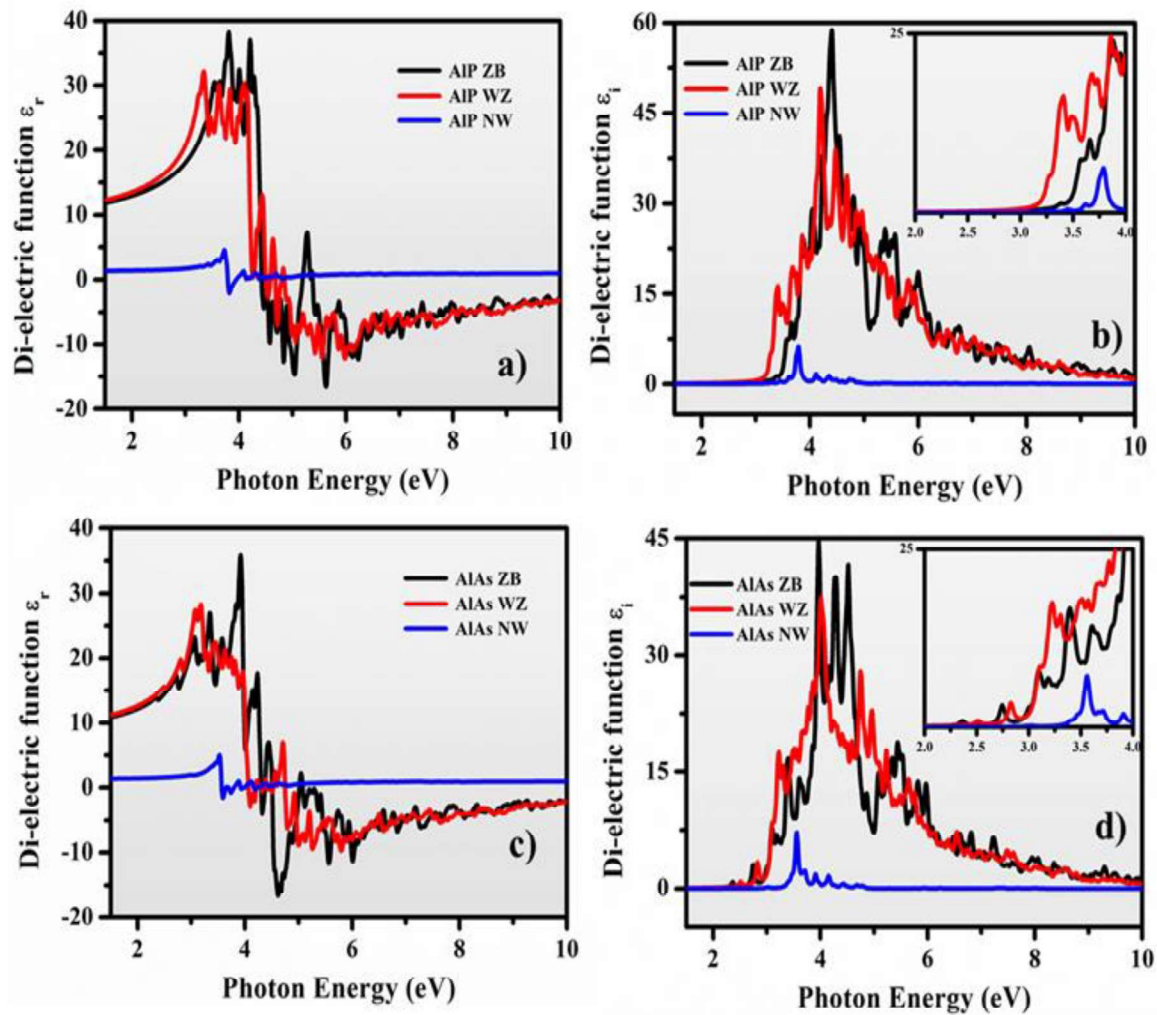


Figure 5.6. Real (ϵ_r) and imaginary (ϵ_i) components of complex di-electric function for aluminium phosphide (AlP) and aluminium arsenide (AlAs) in cubic zincblende (ZB), hexagonal Wurtzite (WZ) and nanowire (NW) configurations.

In case of real part of complex di-electric function that accounts for non-linear optical phenomena, it can be clearly observed that the two-dimensional quantum confinement strongly affects the di-electric function; the reduction in the intensity of the function in both cases validates this observation. Utilizing the computed

components of the complex di-electric functions, further optical properties like absorption co-efficient and joint density of states (JDOS) are calculated. The computed absorption co-efficient of the systems under bulk and NW configurations validate the results on imaginary component of di-electric function and clearly indicate that the AlX compounds under bulk polytypic phases show strong absorption of optical photons, while in case of NW configurations, both systems show peak absorption near extreme end of optical spectra to the ultraviolet regime (see Figs. 5.7(a) and (c)). To infer the same, the joint density of states (JDOS) plots of the systems are computed. It is well-known that the JDOS and absorption have inverse relation, thereby we can

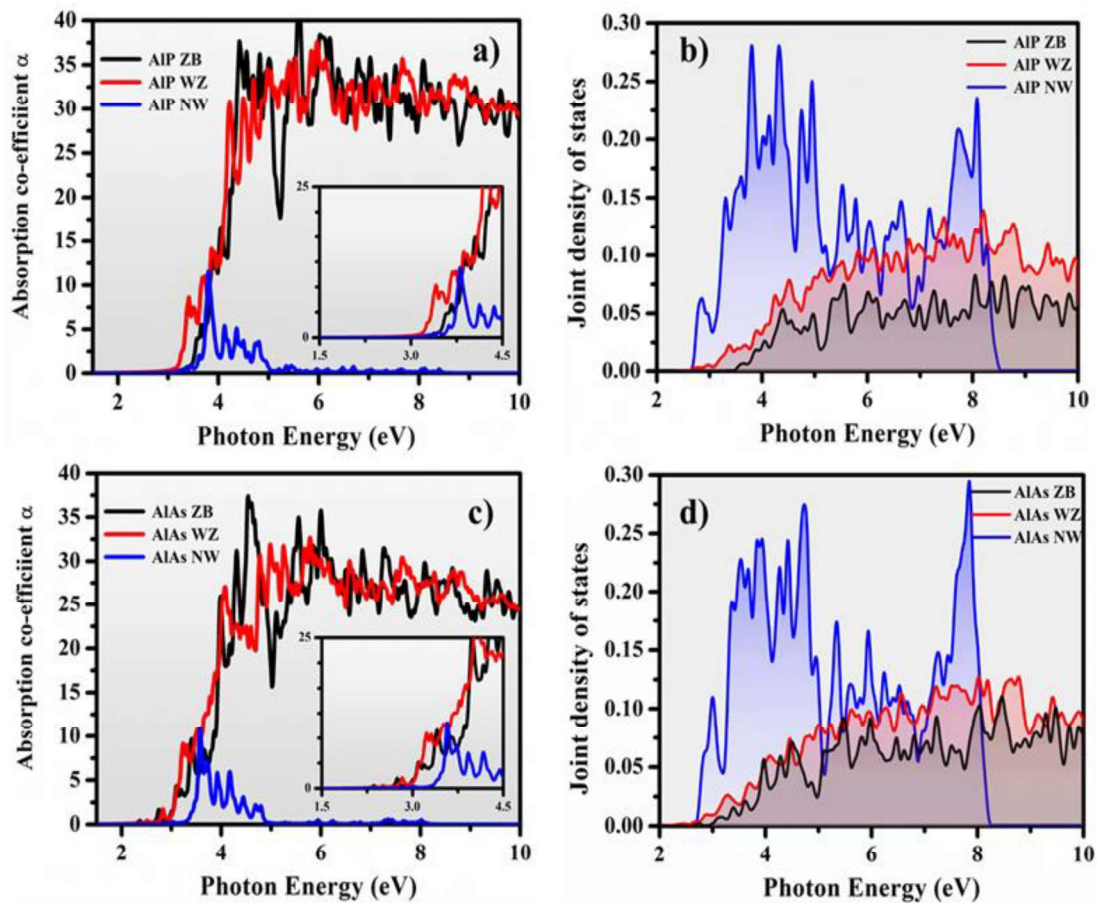


Figure 5.7. Absorption co-efficient (α) and joint density of states (JDOS) as a function of photon energy for aluminium phosphide (AIP) and aluminium arsenide (AlAs) in cubic zincblende (ZB), hexagonal Wurtzite (WZ) and nanowire (NW) configurations.

clearly infer from the Figs. 5.7(b) and (d) that the systems that possess high density might have less absorption capacity and vice-versa. The NWs of both systems possess very high intensity in JDOS plots thereby indicating low capacity of absorption; this fact can be resembled by the lower intensity of absorption co-efficient α of the NW systems as compared to their bulk counterparts (see Figs. 5.7(a) and (c)).

5.3.2 Heterostructure Nanowire

After understanding the properties of the aluminium phosphide (AIP) and aluminium arsenide (AIAs) independently in their bulk and NW configurations, we now turn our attention towards the combined properties of the systems, i.e. the merger of the two systems so as to form one-dimensional (1D) heterostructure nanowire (HSNW) configuration. There are two possibilities of combining the NWs to form a HSNW: (i) covering one NW radially with another so as to have a core/shell like radial HSNW and (ii) stacking two or more NWs on each other on a fixed axis so as to form axial HSNW. We have studied in total three different HSNWs, (a) AIP/AIAs and AIAs/AIP radial (R) HSNWs and, (b) AIP/AIAs axial (A) HSNW.

5.3.2.1 Structural Properties

In the present study, we have constructed two kinds of heterostructures using optimized crystal structures of the AIP and AIAs NWs. To form a heterostructure, the first condition is that the hetero-materials should possess minimum lattice mismatch so as to eliminate generation of strain near the hetero-interface; however, the 1D HSs, have the ability to release strain in radial directions thereby suggesting possibility of growing heterostructures from different materials with large lattice mismatch.³³ In case of AIP and AIAs NWs, the lattice difference is of 0.37 Å (see Table 5.1) that can be

easily accommodated by the neighbouring surface atoms so as to keep the structure energetically stable. The construction and optimization of the HSNWs have been done as per the methodology discussed in **Computational Details** section (see section 5.2). Figure 5.8 depicts the optimized crystal structures of three HSNWs; Fig. 5.8 (a) and (b) show the optimized configurations of AIP/AIAs (R) and AIAs/AIP (R) radial HSNWs, and Fig. 5.8 (c) represents the optimized configuration of AIP/AIAs (A) axial HSNW.

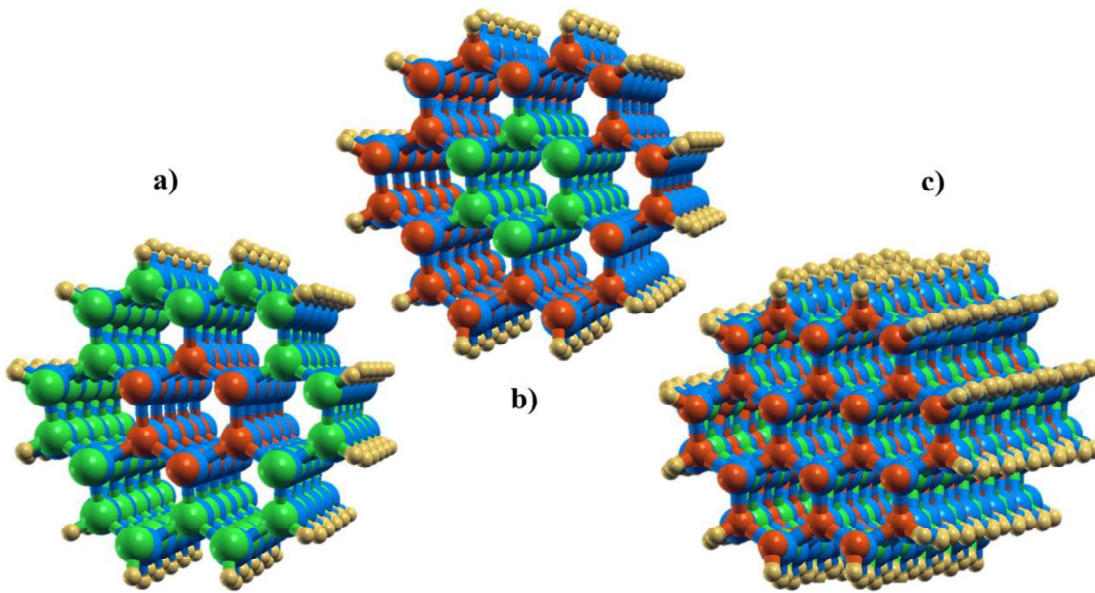


Figure 5.8. Optimized crystal structures of radial heterostructure nanowires (HSNWs) with core/shell geometry (a) AIP/AIAs (R) and (b) AIAs/AIP (R) and, (c) axial HSNW AIP/AIAs (A) with AIP and AIAs NWs stacked on top of each other. The atoms in blue, brown, green and yellow represent respectively the atoms of aluminium, phosphorous, arsenic and hydrogen.

The energetic stability of the HSNWs is assessed by computing energy of cohesion, and, as it can be observed from Table 5.1, the energy of cohesion for all three HSNWs is positive and comparable to NW counterparts. In case of R-HSNWs, it is observed that the AIAs/AIP (R) configuration is more stable than the AIP/AIAs (R); the reason could be the higher ability of AIP-shell NW to accommodate the strain generated by the AIAs-core NW.

5.3.2.2 Electronic Properties

Moving towards the electronic profiles of the HSNWs, it is expected to have a hetero-interface with spatial band alignment so as to achieve high efficiency and controllable carrier dynamics. Apart from the bandgap of the HSNW, it is very important to investigate the contributions of individual hetero-layer to the overall electronic properties. Decomposition of such contributions give clear insight to type of bandgap together with the band off-sets at the hetero-interface that plays a key role in optimizing the carrier dynamics. We have first computed the electronic band dispersion along the high-symmetry k-path $Z \rightarrow \Gamma$, followed by computation of individual hetero-layer contribution to electronic dispersion of the HSNW. Figure 5.9 shows the computed band structure of the three HSNWs which clearly depicts that the AIAs/AIP (R) and AIP/AIAs (A) HSNWs possess direct electronic band gap with gap magnitude of 2.71 and 2.74 eV, respectively. These two properties indicate that the HSNWs are capable of absorbing high energy optical photons thereby qualifying them to be suitable for optoelectronic and photovoltaic devices. In case of AIP/AIAs (R) HSNW, the gap magnitude is desirable yet, the nature of the gap keeps it away from directly qualifying for optical devices. Apart from electronic bandgap, the electronic dispersion reflects the probable charge carrier dynamics of the system. In present case, it can be observed that the axial HSNW possesses very low dispersion in both valence band and conduction band regimes, whereas, in case of the radial HSNWs, the electronic dispersion is quite pronounced. The carrier effective mass that can be determined from these dispersions are lower than their respective bulk counterparts. This could be subjected to the presence of flat bands near the electronic

edge states (see Fig. 5.9). The reduction in carrier effective mass may result in enhancement of the carrier mobility; however, the carrier mobility is not solely dependent on the effective mass, rather it crucially depends on the surface scattering and chemical environment (defects/doping) in the case of such nanostructures.^{34,35}

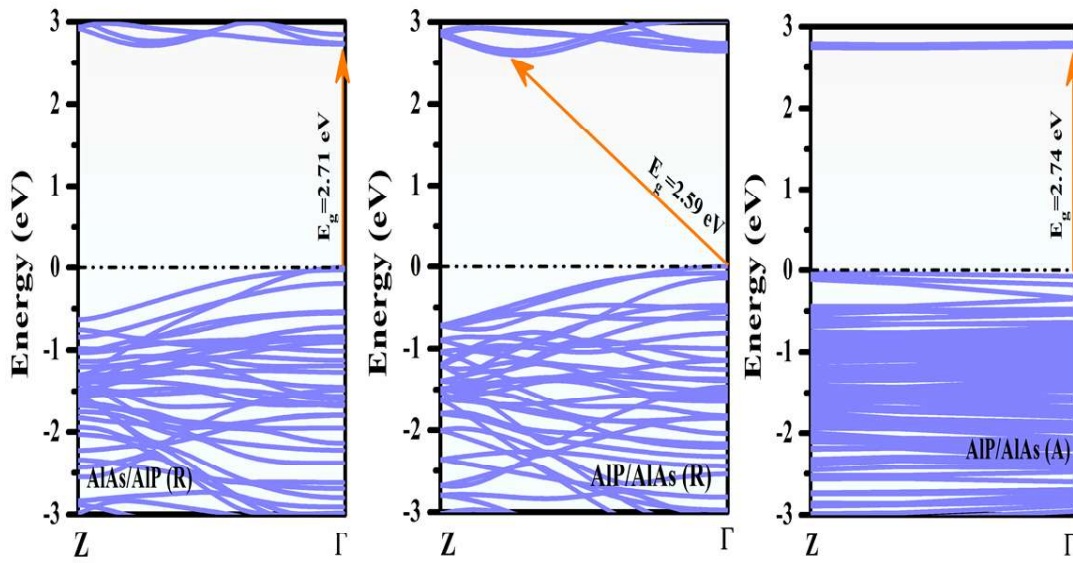


Figure 5.9. Computed electronic band structure for radial (R) heterostructure nanowires (HSNWs) with core/shell geometry AIP/AIAs (R) and AIAs/AIP (R), and, axial HSNW AIP/AIAs (A) with AIP and AIAs NWs stacked on top of one-another.

After understanding the overall electronic dispersion of the AlX compounds under HS configurations, we then decomposed the electronic band structure into hetero-layers to study the contribution of individual materials to the total electronic transport. Figure 5.10 shows the electronic dispersion curves of the constituent hetero-layers of the HSNWs. As it can be observed from the figure, the alignment of the electronic band edges in all three cases gives rise to type-II heterostructure (see Fig. 5.10 (a-c)) which is of utmost importance in case of optoelectronic and photovoltaic devices. This kind of alignment provides opportunity to increase the carrier lifetime

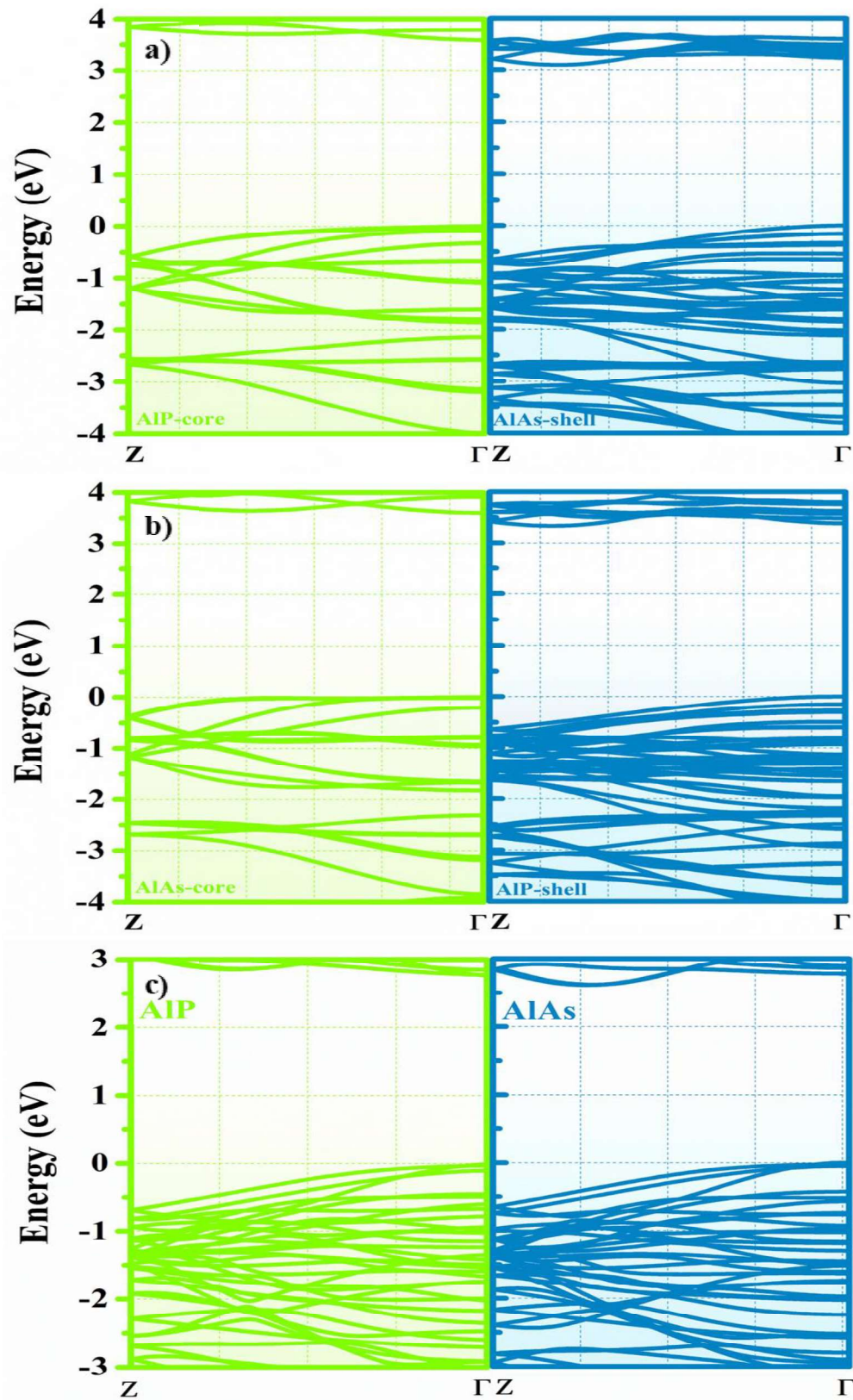


Figure 5.10. Computed electronic band structures of individual heterolayer core/shell for radial (R) heterostructure nanowires (HSNWs) (a) AIP/AlAs, (b) AlAs/AIP and, (c) AIP/AlAs (A) HSNW with bottom/top stacking of heterolayers.

thereby reducing the carrier recombination rate. This happens due to trapping of opposite charge carriers in the separate heterolayers, and as a result, the overall efficiency of the system increases.^{36,37}

5.3.2.3 Optical Properties

The type-II band alignment as observed in the all three cases of HSNWs give motivation to compute and assess the optical transport through the heterostructures. Akin to the bulk and NW systems, the optical properties of the HSNWs is computed under RPA approach. Figure 5.11 represents the computed optical properties of the HSNWs; as it can be observed, the intensity of the imaginary components of the complex di-electric function attains prominent magnitude after 2.5 eV suggesting absorption of high-energy optic photons (see Fig. 5.11 (b)). Out of the three systems, as expected the AIAs/AIP (R) HSNW shows promising trend, which can be confirmed from the profiles of the absorption co-efficient of the system (see Fig. 5.11 (c)). The AIAs/AIP (R) HSNW, apart from moderate bandgap possesses direct nature that aids in radiative recombination phenomena,³⁸ while in case of AIP/AIAs (R) HSNW, intensity is quite suppressed due to contribution of non-radiative processes. This is attributed to the indirect nature of the electronic bandgap of the HSNW (see Fig. 5.9 (b)). As far as the axial HSNW is concerned, the absorption intensity acquires significant magnitude at higher energy scale indicating absorption of high-energy optic and ultraviolet photons. This result is in the anticipation of quite higher bandgap of the HSNW (see Fig. 5.9(c)). To support these results the JDOS plots are calculated, with which the absorption profiles are inversely related. As it can be observed in the Fig. 5.11 (d), the JDOS curve of the AIAs/AIP (R) HSNW is suppressed from the

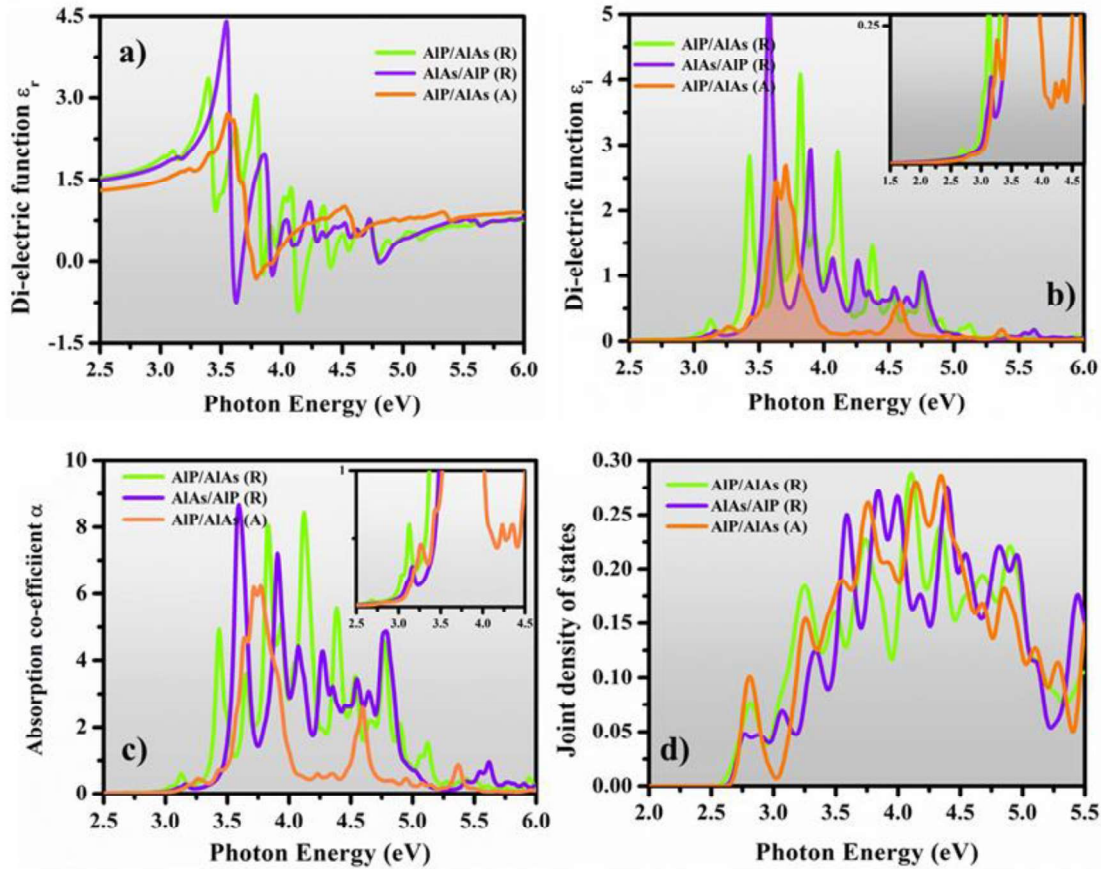


Figure 5.11. Real (ϵ_r) and imaginary (ϵ_i) components of complex di-electric function (a, b), absorption co-efficient α (c) and joint density of states (JDOS) (d) for AIP/AlAs and AlAs/AIP radial (R) heterostructure nanowires (HSNWs) and AIP/AlAs axial (A) HSNW configurations.

remaining two systems indicating its higher capacity of absorption. The other two systems show quite higher JDOS population thereby confirming their capacity to absorb photons from extreme end of the optic spectra.

5.4 Conclusion

The *first-principles* calculations of the electro-optic properties of AIX (X=P, As) compounds under bulk and nanostructured configurations based on DFT is performed. The considered bulk phases, cubic ZB and hexagonal WZ of both compounds show indirect nature of electronic bandgap. Interestingly, on imposition

of two-dimensional quantum confinement results in transition of electronic bandgap from indirect to direct in case of AlP. As expected, the enhancement in the electronic gap is observed in both compounds under nanowire configuration. As the electronic bandgap that was 1.39/1.78 eV and 1.35/1.67 eV in case of the bulk configurations of AlP and AlAs (ZB/WZ), gets enhanced to 2.74 and 2.61 eV for AlP and AlAs NWs, respectively. These gaps lie within the visible to extreme end of optical regime of the electro-magnetic spectrum indicating the absorption of visible-to-high energy photons by the systems. The computed absorption co-efficient profile of the systems support this observation. In case of AlP NW, the electronic and optical bandgaps are same subjected to direct electronic bandgap, thereby providing complete radiative response. Moving towards the most crucial part of the study, i.e. formation of heterostructure nanowire (HSNW) from the two distinct NWs, the HSNWs of both types (radial (R)/axial(A)) were constructed and investigated. In case of radial HSNWs with core/shell geometry both systems, AlP/AlAs and AlAs/AlP HSNWs possess type-II band alignment which is of utmost importance in case of optical devices. As far as gap magnitude is concerned, both HSNWs possess the gap between 2.5 to 2.7 eV indicating their application as high-energy photon absorber layers; furthermore, in case of AlAs/AlP HSNW, the direct nature of bandgap suggests its potential as an efficient photo-absorber. Assessing the results in case of axial HSNW, the gap magnitude of 2.74 eV indicate its utilization as wide bandgap semi-conductor for tandem solar cells. The bandgap alignment in all three cases is of type-II, indicating their vital role in separation of charge carriers in separate layers. This technique aids in increasing the carrier recombination rates by modifying their life-times and

diffusion lengths. This study suggests possibility of utilizing earth abundant and robust aluminium based group-V materials in the optical and PV industry. The incorporation of aluminium in such devices will not only be cost-effective and promising efficiencies, but also will provide solutions to protect the materials from corrosion, oxidative and harsh chemical environments. The present study gives insight to the electro-optic responses of the AlX (X=P/As) materials within the bulk polytypic phases, NW and HSNW regimes thereby drawing a clear picture of the electro-optic transport through these materials. The transition from bulk to NW to HSNW could be an efficient pathway to tune these responses so as to achieve promising outcomes.

References

- (1) Wong-Leung, J.; Yang, I.; Li, Z.; Karuturi, S. K.; Fu, L.; Tan, H. H.; Jagadish, C. Engineering III-V Semiconductor Nanowires for Device Applications. *Adv. Mater.* **2020**, *32* (18), 1-14. <https://doi.org/10.1002/adma.201904359>.
- (2) Tournet, J.; Lee, Y.; Karuturi, S. K.; Tan, H. H.; Jagadish, C. III-V Semiconductor Materials for Solar Hydrogen Production: Status and Prospects. *ACS Energy Lett.* **2020**, *5* (2), 611-622. <https://doi.org/10.1021/acsenenergylett.9b02582>.
- (3) Li, Z.; Kim, T. H.; Han, S. Y.; Yun, Y. J.; Jeong, S.; Jo, B.; Ok, S. A.; Yim, W.; Lee, S. H.; Kim, K.; et al. Wide-Bandgap Perovskite/Gallium Arsenide Tandem Solar Cells. *Adv. Energy Mater.* **2020**, *10* (6), 1-16. <https://doi.org/10.1002/aenm.201903085>.
- (4) Shur, M. Wide Band Gap Semiconductor Technology: State-of-the-Art. *Solid. State. Electron.* **2019**, *155* (March), 65-75. <https://doi.org/10.1016/j.sse.2019.03.020>.
- (5) Barrigón, E.; Heurlin, M.; Bi, Z.; Monemar, B.; Samuelson, L. Synthesis and Applications of III-V Nanowires. *Chem. Rev.* **2019**, *119* (15), 9170-9220. <https://doi.org/10.1021/acs.chemrev.9b00075>.
- (6) Boras, G.; Yu, X.; Liu, H. III-V Ternary Nanowires on Si Substrates: Growth, Characterization and Device Applications. *J. Semicond.* **2019**, *40* (10), 101301. <https://doi.org/10.1088/1674-4926/40/10/101301>.
- (7) Nakamura, S.; Senoh, M.; Mukai, T. P-Gan/n-Ingan/n-Gan Double-Heterostructure Blue-Light-Emitting Diodes. *Jpn. J. Appl. Phys.* **1993**, *32* (1 A), L8-L11.

- <https://doi.org/10.1143/JJAP.32.L8>.
- (8) Givargizov, E. I. Fundamental Aspects of VLS Growth. *J. Cryst. Growth* **1975**, 31 (C), 20–30. [https://doi.org/10.1016/0022-0248\(75\)90105-0](https://doi.org/10.1016/0022-0248(75)90105-0).
 - (9) Haraguchi, K.; Katsuyama, T.; Hiruma, K.; Ogawa, K. GaAs P-n Junction Formed in Quantum Wire Crystals. *Appl. Phys. Lett.* **1992**, 60 (6), 745–747. <https://doi.org/10.1063/1.106556>.
 - (10) Lalngaihawmi, R.; Vanlalruata, B.; Shankar, A.; Rai, D. P.; Sandeep; Thapa, R. K. Study of Aluminium Pnictides by Using Full Potential Linearized Augmented Plane Wave (FP-LAPW) Method. *AIP Conf. Proc.* **2015**, 1661 (May). <https://doi.org/10.1063/1.4915365>.
 - (11) Malsawmtluanga, A.; Ralte, R. L.; Pachuau, Z. Study of Electronic and Optical Properties of Aluminium Pnictides (AlX, X = P, As, Sb). **2014**, 14 (4), 195–199.
 - (12) Vurgaftman, I.; Meyer, J. R.; Ram-Mohan, L. R. Band Parameters for III-V Compound Semiconductors and Their Alloys. *J. Appl. Phys.* **2001**, 89 (11 I), 5815–5875. <https://doi.org/10.1063/1.1368156>.
 - (13) Benyahia, N.; Zaoui, A.; Madouri, D.; Ferhat, M. Dynamic Properties of III-V Polytypes from Density-Functional Theory. *J. Appl. Phys.* **2017**, 121 (12). <https://doi.org/10.1063/1.4979011>.
 - (14) Jiang, M.; Xiao, H. Y.; Peng, S. M.; Yang, G. X.; Liu, Z. J.; Zu, X. T. A Comparative Study of Low Energy Radiation Response of AlAs, GaAs and GaAs/AlAs Superlattice and the Damage Effects on Their Electronic Structures. *Sci. Rep.* **2018**, 8 (1), 1–15. <https://doi.org/10.1038/s41598-018-20155-0>.
 - (15) Chandiramouli, R.; Rubalya Valentina, S.; Nagarajan, V. Band Structure Engineering and Transport Properties of Aluminium Phosphide Nanoribbon - A First-Principles Study. *Superlattices Microstruct.* **2014**, 76, 135–148. <https://doi.org/10.1016/j.spmi.2014.10.013>.
 - (16) De, A.; Pryor, C. E. Predicted Band Structures of III-V Semiconductors in the Wurtzite Phase. *Phys. Rev. B - Condens. Matter Mater. Phys.* **2010**, 81 (15). <https://doi.org/10.1103/PhysRevB.81.155210>.
 - (17) Juntunen, T.; Koskinen, T.; Khayrudinov, V.; Haggren, T.; Jiang, H.; Lipsanen, H.; Tittonen, I. Thermal Conductivity Suppression in GaAs-AlAs Core-Shell Nanowire Arrays. *Nanoscale* **2019**, 11 (43), 20507–20513. <https://doi.org/10.1039/c9nr06831g>.
 - (18) Borgström, M. T.; Mergenthaler, K.; Messing, M. E.; Håkanson, U.; Wallentin, J.; Samuelson, L.; Pistol, M. E. Fabrication and Characterization of AlP-GaP Core-Shell Nanowires. *J. Cryst. Growth* **2011**, 324 (1), 290–295. <https://doi.org/10.1016/j.jcrysgro.2011.03.055>.

- (19) Publications, O. (12) United States Patent. **2019**, 2 (12). <https://doi.org/10.1016/j.Snb.2006>.
- (20) Beg, S.; Saeed, S. H.; Siddiqui, M. J. III-V Compound Semiconductor Laser Heterostructures Parametric Performance Evaluation For InGaAs/GaAs And AlGaAs/GaAs. *Adv. Comput. Sci. Technol.* **2017**, 10 (10), 2985–3013.
- (21) Glas, F.; Harmand, J. C.; Patriarche, G. Why Does Wurtzite Form in Nanowires of III-V Zinc Blende Semiconductors? *Phys. Rev. Lett.* **2007**, 99 (14). <https://doi.org/10.1103/PhysRevLett.99.146101>.
- (22) Johansson, J.; Bolinsson, J.; Ek, M.; Caroff, P.; Dick, K. A. Combinatorial Approaches to Understanding Polytypism in III-V Nanowires. *ACS Nano* **2012**, 6 (7), 6142–6149. <https://doi.org/10.1021/nn301477x>.
- (23) Dabhi, S. D.; Jha, P. K. Ab Initio Study of Strained Wurtzite InAs Nanowires: Engineering an Indirect-Direct Band Gap Transition through Size and Uniaxial Strain. *RSC Adv.* **2015**, 5 (109), 89993–90000. <https://doi.org/10.1039/c5ra16512a>.
- (24) Dabhi, S. D.; Jha, P. K. First-Principles Study for Thermodynamic Properties of Wurtzite Indium Pnictides. *J. Therm. Anal. Calorim.* **2016**, 124 (3), 1341–1347. <https://doi.org/10.1007/s10973-016-5298-9>.
- (25) Gajaria, T. K.; Dabhi, S. D.; Jha, P. K. Ab Initio Energetics and Thermoelectric Profiles of Gallium Pnictide Polytypes. *Sci. Rep.* **2019**, 9 (1). <https://doi.org/10.1038/s41598-019-41982-9>.
- (26) Apblett, A. W. Aluminum: Inorganic Chemistry. *Encycl. Inorg. Bioinorg. Chem.* **2011**, 3. <https://doi.org/10.1002/9781119951438.eibc0007>.
- (27) Kohn, W.; Sham, L. J. Self-Consistent Equations Including Exchange and Correlation Effects. *Phys. Rev.* **1965**, 140 (4A). <https://doi.org/10.1103/PhysRev.140.A1133>.
- (28) Perdew, J. P.; Zunger, A. Self-Interaction Correction to Density-Functional Approximations for Many-Electron Systems. *Phys. Rev. B* **1981**, 23 (10), 5048–5079. <https://doi.org/10.1103/PhysRevB.23.5048>.
- (29) Monkhorst, H. J.; Pack, J. D. Special Points for Brillouin-Zone Integrations. *Phys. Rev. B* **1976**, 13 (12), 5188–5192. <https://doi.org/10.1103/PhysRevB.13.5188>.
- (30) Gajdoš, M.; Hummer, K.; Kresse, G.; Furthmüller, J.; Bechstedt, F. Linear Optical Properties in the Projector-Augmented Wave Methodology. *Phys. Rev. B - Condens. Matter Mater. Phys.* **2006**, 73 (4). <https://doi.org/10.1103/PhysRevB.73.045112>.
- (31) Harl, J.; Kresse, G.; Sun, L. D.; Hohage, M.; Zeppenfeld, P. Ab Initio Reflectance Difference Spectra of the Bare and Adsorbate Covered Cu(110) Surfaces. *Phys. Rev. B - Condens. Matter Mater. Phys.* **2007**, 76 (3). <https://doi.org/10.1103/PhysRevB.76.035436>.

- (32) Wang, S. Q.; Ye, H. Q. A Plane-Wave Pseudopotential Study on III-V Zinc-Blende and Wurtzite Semiconductors under Pressure. *J. Phys. Condens. Matter* **2002**, *14* (41), 9579–9587. <https://doi.org/10.1088/0953-8984/14/41/313>.
- (33) Caroff, P.; Messing, M. E.; Mattias Borg, B.; Dick, K. A.; Deppert, K.; Wernersson, L. E. InSb Heterostructure Nanowires: MOVPE Growth under Extreme Lattice Mismatch. *Nanotechnology* **2009**, *20* (49), 495606. <https://doi.org/10.1088/0957-4484/20/49/495606>.
- (34) Dos Santos, C. L.; Piquini, P.; Lima, E. N.; Schmidt, T. M. Low Hole Effective Mass in Thin InAs Nanowires. *Appl. Phys. Lett.* **2010**, *96* (4), 1–4. <https://doi.org/10.1063/1.3280048>.
- (35) Jiang, X.; Xiong, Q.; Nam, S.; Qian, F.; Li, Y.; Lieber, C. M. InAs/InP Radial Nanowire Heterostructures as High Electron Mobility Devices. *Nano Lett.* **2007**, *7* (10), 3214–3218. <https://doi.org/10.1021/nl072024a>.
- (36) Long, C.; Dai, Y.; Gong, Z. R.; Jin, H. Robust Type-II Band Alignment in Janus-MoSSe Bilayer with Extremely Long Carrier Lifetime Induced by the Intrinsic Electric Field. *Phys. Rev. B* **2019**, *99* (11), 1–7. <https://doi.org/10.1103/PhysRevB.99.115316>.
- (37) Shamirzaev, T. S.; Debus, J.; Yakovlev, D. R.; Glazov, M. M.; Ivchenko, E. L.; Bayer, M. Dynamics of Exciton Recombination in Strong Magnetic Fields in Ultrathin GaAs/AlAs Quantum Wells with Indirect Band Gap and Type-II Band Alignment. *Phys. Rev. B* **2016**, *94* (4), 1–10. <https://doi.org/10.1103/PhysRevB.94.045411>.
- (38) Zhang, X.; Shen, J. X.; Wang, W.; Van De Walle, C. G. First-Principles Analysis of Radiative Recombination in Lead-Halide Perovskites. *ACS Energy Lett.* **2018**, *3* (10), 2329–2334. <https://doi.org/10.1021/acsenergylett.8b01297>.
-

CHAPTER 6

PHOSPHIDE NANOWIRES FOR PHOTOCATALYTIC APPLICATION